The Astronomical Journal, 154:44 (16pp), 2017 August https://doi.org/10.3847/1538-3881/aa78a5

Scattering Properties of the Venusian Clouds Observed by the UV Imager on board *Akatsuki*

Y. J. Lee[1], A. Yamazaki[1], T. Imamura[2], M. Yamada[3], S. Watanabe[4], T. M. Sato[1], K. Ogohara[5], G. L. Hashimoto[6], and S. Murakami[1]
[1] Institute of Space and Astronautical Science, Japan Aerospace Exploration Agency, 3-1-1 Yoshinodai, Chuoku, Sagamihara, Kanagawa 252-5210, Japan; leeyj@ac.jaxa.jp
[2] The University of Tokyo, 5-1-5 Kashiwanoha, Kashiwa, Chiba 277-8561, Japan
[3] Planetary Exploration Research Center, Chiba Institute of Technology, 2-17-1, Tsudanuma, Narashino, Chiba 275-0016, Japan
[4] Hokkaido Information University, 59-2 Nishinopporo, Ebetsu, Hokkaido 069-0832, Japan
[5] University of Shiga Prefecture, 2500 Hassaka, Hikone, Shiga 522-8533, Japan
[6] Department of Earth Sciences, Okayama University, 3-1-1 Tsushimanaka, Kita, Okayama 700-8530, Japan
Received 2017 March 21; revised 2017 June 9; accepted 2017 June 9; published 2017 July 6

Abstract

We analyze the albedo of Venus obtained from the UV Imager on board *Akatsuki*. A relative global mean albedo over phase angle is used in this study, and we confirm the glory feature at 283 and 365 nm in the data acquired in 2016 May. We successfully simulate the observation using a radiative transfer model. Our results show that cloud aerosols of $r_{\rm eff} = 1.26$ μm and $v_{\rm eff} = 0.076$ (mode 2) can explain the glory, consistent with a property of aerosols previously suggested by using the Venus Monitoring Camera on board *Venus Express*. We find that SO_2 and the unknown UV absorber are necessary factors to explain the decreasing trend of the observed relative albedo at phase angles larger than 10°. We suggest a range of possible SO_2 abundance from 80 to 400 ppbv at the cloud top level, depending on atmospheric conditions assumed.

Key words: planets and satellites: atmospheres – ultraviolet: planetary systems

1. Introduction

Venus in the ultraviolet (UV) range reveals dark and bright contrasts. Since their discovery in the 1920s (Wright 1927; Ross 1928), dark UV features have been understood to be mainly due to absorptions by SO_2 and a so-called unknown UV absorber near the cloud top level (Travis 1975; Pollack et al. 1980; Titov et al. 2013). While the absorption spectrum of SO_2 is well constrained (Bogumil et al. 2003; Vandaele et al. 2009), that of the unknown UV absorber is not yet well understood and displays a rather broad absorption shape with its maximum around 360–370 nm. This makes it difficult to identify a specific source of absorption, but there are a number of possible candidates, i.e., S_x, $FeCl_3$, OSSO, etc. (Zasova et al. 1981; Toon et al. 1982; Mills et al. 2007; Frandsen et al. 2016; Krasnopolsky 2017). On the other hand, clouds and upper haze aerosols are effective scatterers of incident solar radiance, so bright features would correspond to fewer UV absorbers and/or be shrouded by the cloud aerosols.

Mie scattering by the cloud aerosols causes strong forward and backward scatterings (Mallama et al. 2006; Lee et al. 2015; Shalygina et al. 2015). Particularly in the backward scattering, Markiewicz et al. (2014) reported the observation of a glory on Venus for the first time, showing its circular shape in close-up images in UV, visible, and infrared channels taken by the Venus Monitoring Camera (VMC) on board *Venus Express*. Petrova et al. (2015a, 2015b) analyzed VMC images in detail and determined microphysical properties of the cloud aerosols: the effective variance ($v_{\rm eff}$) of 0.07 and the effective radius ($r_{\rm eff}$) of 0.8–1.6 μm. The glory on Venus had also been recognized in images taken from far away, even from the ground. In such cases, disk-integrated albedo/flux had been used to detect the glory (García Muñoz et al. 2014; Satoh et al. 2015).

On the other hand, it is important to understand the spatial and temporal variations of the UV absorbers because they—i.e., SO_2 and the unknown UV absorber—are expected to provide important clues to the sulfur cycle in the Venusian atmosphere and radiative energy balance in the mesosphere, respectively (Mills et al. 2007; Titov et al. 2013). Also it is worth noting that previous studies revealed temporal variations of the UV absorbers and their correlations with each other (Marcq et al. 2013; Lee et al. 2015). This suggests changes in the dynamics of the Venusian mesosphere, or a source of sulfur, which is related to volcanic activities.

The Venus orbiter *Akatsuki* has been monitoring the atmosphere of Venus since 2015 December (Nakamura et al. 2016), as a successor to *Venus Express* (2006–2014). This provides us with a unique chance to understand the temporal and spatial variations of the UV absorbers using the UVI Imager (UVI) on board *Akatsuki*. This is a challenging task, because without a spectrometer we cannot fit absorption or continuum spectral features, but we need to estimate absorptions at a specific wavelength. In this study, we show that this is possible, but indirectly, using the dependence of scattering properties on phase angle. We select images (Section 2) and perform photometric correction (Section 3). We show phase curves in the 283 and 365 nm channels in Section 4. Note that this is the first time that the phase curve of Venus in the 283 nm channel has been presented in the history of Venus observation. A relative albedo is analyzed to understand the glory feature (Section 4). We investigate further, suggesting possible combinations of scatterings and absorptions that can explain the phase curves qualitatively (Section 4).

2. Data

Akatsuki is the first Japanese orbiter of Venus; it was launched in 2010 and succeeded in its orbital insertion in 2015 (Nakamura et al. 2016). *Akatsuki* has a highly elliptical equatorial orbit, and its orbital period has been adjusted for its maintenance and scientific performance. Since 2016 April 4, *Akatsuki* has orbited Venus every 10.8 Earth days, and the

distance of *Akatsuki* from the center of Venus varies from ~370,000 km at apocenter to ~7000–18,000 km at pericenter. The apparent diameter of Venus also changes according to the distance, from about 2° to larger than 12°. *Akatsuki* moves slowly near apocenter, so the size of Venus is less than 3° during 73% of one orbit (~8 Earth days), which can allow global monitoring. Close-up imaging is possible for ~7 hr near pericenter. Therefore, although *Akatsuki* passes the dayside and nightside of Venus in every orbit, global monitoring of the dayside is possible when the apocenter of *Akatsuki*'s orbit is located above it. Such a period continues for about four Earth months, then alters to global monitoring of the nightside for the same duration. This alternation is due to the rotation of Venus around the Sun (period ~ 225 Earth days), while the major axis of *Akatsuki*'s orbit is fixed to the inertial frame of the solar system. Consequently, a period of dayside global monitoring took place from 2016 April to July. UVI could observe Venus at small solar phase angles—less than 30°—in May and June. However, *Akatsuki* was not able to make observations of Venus for a week at the beginning of June, due to the limitation of the telecommunication between the ground and *Akatsuki* during a superior conjunction around 2016 June 6. Therefore, the data in May cover the small solar phase angles well.

UVI is one of six instruments on board *Akatsuki*. It has a field of view of 12° and an image sensor of 1024 × 1024 pixels. The spatial resolution of Venus images at a sub-spacecraft point changes from ~80 km pix^{-1} at apocenter to 0.18–2.4 km pix^{-1} at pericenter. UVI performs observations well despite the longer cruising time than initially planned, and acquired images are in good shape as shown in the first image after Venus orbit insertion(Nakamura et al. 2016). UVI has two channels centered at wavelengths of 283 and 365 nm, targeting SO_2 and the unknown UV absorber, respectively. Imaging is done sequentially: an image is taken at 283 nm first, and one is taken at 365 nm 4 minutes later. This imaging in pairs is designed to compare SO_2 and the unknown UV absorber simultaneously. The time interval from one pair of images to the next is usually 2 hr. This can be continuous except for the time required for telecommunication with the ground. So up to ~8 pairs of Venus images could be taken per Earth day.

In this manuscript, we analyze dayside global images. We selected images according to the following conditions. First, an image contains the full visible area of the dayside of Venus in the field of view of UVI. Second, an image has a complete shape without any missing data or noise, which are caused by the decompression process on the ground and insufficient data transmission from the spacecraft. Third, a limb-fitting process has been successfully completed, providing accurate geometric information. The limb-fitting process is a technique to correct SPICE-based geometric information as described in Ogohara et al. (2012). This ensures high accuracies of angles of emergence and incidence from the limb to near the terminator. Finally, we analyze 801 images in both channels, which were taken from 2015 December 7 to 2016 August 11. We use all of the images for statistical investigation of photometric corrections (see Section 3.1) over a broad range of solar phase angles from 0 to 140°. The images taken in 2016 May become our major target for understanding scattering properties of the Venusian clouds (see Section 4).

2.1. UVI Sensor and Data Processing

The UVI sensor is composed of a charge-coupled device (CCD), a filter wheel, and optics. The back-illuminated CCD is used without antiblooming structures, so this increases sensitivity over the image area of 13.3 × 13.3 mm. There are four channels on the rotation filter wheel: shutter, diffuser, and 283 and 365 nm bandpass filters. Scientific data indicate images taken with the 283 and 365 nm filters. Typical exposure times are 46 ms at 365 nm, and 250 and 500 ms at 283 nm. After a scientific image, a 0 s exposure image is taken. The latter is subtracted from the scientific image on board, correcting smear noise. Dark signal is removed also on board using a shutter image. A typical signal-to-noise ratio is over 100 for both channels after these onboard processes. Then, all images are compressed using a fast lossless image compression method, HIREW (Takada et al. 2007), and transmitted to the ground.

A flat-field correction is done on the ground. This study uses the flat-field data taken from an integrating sphere experiment using the flight model in 2009, before the spacecraft's launch. We measured the flat-field of the 365 nm filter. This flat-field is used for both the 283 and 365 nm images, assuming similar conditions for the 283 nm filter.

An absolute calibration of radiance has not been completed yet. Stars were observed several times in 2016, and the data are currently being analyzed. Therefore it is difficult to use absolute albedo, and we decide to use relative albedo instead, which is albedo normalized to that at 30° phase angle (see Section 4).

3. Methods

We perform photometric corrections on UVI images, following the methods described in Lee et al. (2015). We retrieve phase curves of global mean albedo in the two channels. The observed phase curves are compared to one-dimensional radiative transfer model (RTM) calculations.

3.1. Photometric Correction

An observed Venus UV image combines solar radiance scattered by the cloud aerosols and by atmospheric molecules, and absorption markings. The scattered solar radiance smoothly decreases in brightness from a sub-solar point to the terminator, showing a strong dependence on scattering angles, i.e., angles of emergence (e) and incidence (i) and the phase angle (α). Photometric correction is a technique that removes this dependence on scattering angles, and it has been applied for Venus UV images (Molaverdikhani et al. 2012; Titov et al. 2012; Lee et al. 2015).

Each pixel (x, y) of UVI measures radiance, i.e., $R_{\rm obs}(x, y)$. As each pixel has different scattering angles, the measured radiance is a function of these scattering angles, $R_{\rm obs}(\mu, \mu_0, \alpha)$, where $\mu = \cos(e)$ and $\mu_0 = \cos(i)$. We convert the observed radiance into the *radiance factor* ($r_{\rm F}$), a quantity of reflectivity (Hapke 2012). We calculate $r_{\rm F}$ as

$$r_{\rm F,ch}(\mu, \mu_0, \alpha) = \pi R_{\rm obs,ch}(\mu, \mu_0, \alpha)\frac{{d_{\rm V}}^2}{S_{\odot,\rm ch}}, \quad (1)$$

where ch is the channel of UVI, $R_{\rm obs}$ is radiance (W m^{-2} sr^{-1} μm^{-1}), $d_{\rm V}$ is the distance of Venus from the Sun (au), and $S_\odot$ is the averaged solar flux at 1 au. $S_{\odot,\rm ch}$ is

calculated as

$$S_{\odot,\mathrm{ch}} = \frac{\int_\lambda S_{\mathrm{irr}}(\lambda) T_{\mathrm{ch}}(\lambda) d\lambda}{\int_\lambda T_{\mathrm{ch}}(\lambda) d\lambda}, \quad (2)$$

where λ is wavelength (μm), $S_{\mathrm{irr}}(\lambda)$ is the solar irradiance spectrum at 1 au (W m^{-2} μm^{-1}), and T_{ch} is the transmittance profile of the UVI channels. $S_{\mathrm{irr}}(\lambda)$ is taken from the Smithsonian Astrophysical Observatory reference spectrum 2010 (SAO2010) (Chance & Kurucz 2010). We note that $S_\odot$ of the 283 nm channel can be different depending on references for the solar spectrum, for example, 334 W m^{-2} μm^{-1} using SAO2010, and 279 W m^{-2} μm^{-1} using the Whole Heliosphere Interval 2008 (WHI2008) Quiet Sun campaign spectrum (Woods et al. 2009). The latter is 16% smaller than the former. This may need to be discussed if we use an absolute radiance, but is not relevant to this study because we use relative albedo (Section 4).

$r_{\mathrm{F,ch}}$ can be separated into an albedo $A_{\mathrm{ch}}(\alpha)$ and a disk function $D_{\mathrm{ch}}(\mu, \mu_0, \alpha)$ (Shkuratov et al. 2011):

$$r_{\mathrm{F,ch}} = A_{\mathrm{ch}}(\alpha) D_{\mathrm{ch}}(\mu, \mu_0, \alpha). \quad (3)$$

The albedo A_{ch} is a function of phase angle (α) only. The disk function D_{ch} describes the dependence on scattering angles. Here, phase angle (α) is considered as a constant for all pixels. This is a mean value of valid pixels as an approximation, while actual variations of phase angles span from 0.2° to 8° in one image.

Among many photometric laws for D_{ch}, we evaluate three well-known simple photometric laws: the Lambert law, a combined Lambert and Lommel–Seeliger law, and the Minnaert law, the definitions of which are shown in below.

The Lambert law (La):

$$D_{\mathrm{La,ch}} = \mu_0. \quad (4)$$

The combined Lambert and Lommel–Seeliger law (LLS) (Buratti & Veverka 1983; McEwen 1986):

$$D_{\mathrm{LLS,ch}} = k_{\mathrm{LLS,ch}}(\alpha) \frac{2\mu_0}{\mu_0 + \mu} + (1 - k_{\mathrm{LLS,ch}}(\alpha))\mu_0 \quad (5)$$

where $k_{\mathrm{LLS,ch}}(\alpha)$ is the coefficient describing relative contributions of Lambert and Lommel–Seeliger, i.e., 0 is pure Lambert law, and 1 is pure Lommel–Seeliger law. $k_{\mathrm{LLS,ch}}(\alpha)$ can be determined from the observed images using Equations (3) and (5) (the derivation is shown in Lee et al. 2015).

The Minnaert law (Mi):

$$D_{\mathrm{Mi,ch}} = {\mu_0}^{k_{\mathrm{Mi,ch}}(\alpha)} \mu^{k_{\mathrm{Mi,ch}}(\alpha)-1} \quad (6)$$

where $k_{\mathrm{Mi,ch}}(\alpha)$ is the Minnaert index (Hapke 2012). $k_{\mathrm{Mi,ch}}(\alpha)$ is determined from the slope of $\ln(r_{\mathrm{F,ch}}\mu)$ as a function of $\ln(\mu\mu_0)$ (Equations (3) and (6)).

Results of $k_{\mathrm{LLS}}(\alpha)$ and $k_{\mathrm{Mi}}(\alpha)$ determined for the 283 nm channel are shown in Figures 1(a) and (b), respectively. A least-square curve fit of second order is used to determine $k_{\mathrm{LLS,283}}(\alpha)$:

$$k_{\mathrm{LLS,283}}(\alpha) = 0.466450 + 0.00834447\alpha - 9.34261 \times 10^{-5}\alpha^2. \quad (7)$$

A linear least-square fit is used to determine $k_{\mathrm{Mi,283}}(\alpha)$:

$$k_{\mathrm{Mi,283}}(\alpha) = 0.003347\alpha + 0.532352. \quad (8)$$

Using the $k_{\mathrm{LLS,283}}(\alpha)$ and $k_{\mathrm{Mi,283}}(\alpha)$ determined above, we generate three modeled images for each observed image. Correlation coefficients are calculated between observed and modeled radiance factors for the three laws. Figure 1(c) shows the results with varying phase angle α, and the best among the three laws is highlighted for each observed image. In general, D_{LLS} shows the best performance over all α with the highest mean correlation coefficient of 0.9229. D_{Mi} is the next best at 0.8948, and D_{La} is the worst, 0.8314. All the laws show a trend of increasing correlation coefficient as phase angle increases. D_{Mi} performs better than the others at small phase angles.

The same process is repeated for the 365 nm channel. Figure 2(a) shows the results for $k_{\mathrm{LLS,365}}(\alpha)$. The least-square fit (red curve) is

$$k_{\mathrm{LLS,365}}(\alpha) = 0.257086 + 0.00102739\alpha - 1.45403 \times 10^{-5}\alpha^2. \quad (9)$$

$k_{\mathrm{LLS,365}}(\alpha)$ is about half of $k_{\mathrm{LLS,283}}(\alpha)$ at same phase angles. The small $k_{\mathrm{LLS,365}}$ at large phase angles implies a more Lambertian-like curve, but this requires careful consideration of the viewing geometry, because different values had to be used for the 365 nm channel of VMC (Lee et al. 2015). These authors recognized artifacts of a Lambertian in pixels at high angles of incidence and emergence, especially at $\alpha > 90°$, as shown in their Figure 6. This Lambertian artifact could be recognized easily from the VMC images due to abnormal bright features in the equatorial region. However, this would be difficult to notice from the UVI images, because pixels at high angles of emergence and incidence are coincident with regions at high latitude, which are typically brighter than equatorial regions. We consider that the small $k_{\mathrm{LLS,365}}$ may result in artifacts of a Lambertian in the UVI images, but it is difficult to distinguish this from the typical latitudinal distribution of brightness at this moment.

The result for $k_{\mathrm{Mi,365}}(\alpha)$ is

$$k_{\mathrm{Mi,365}}(\alpha) = 0.002109\alpha + 0.755472, \quad (10)$$

as shown in Figure 2(b).

A comparison of the three laws is shown in Figure 2(c). The highest mean correlation coefficient is shown for D_{LLS}, 0.9263; the next best is D_{Mi} at 0.9158, and the least correlation is shown for D_{La}, 0.9083, but the differences are small. We select D_{LLS} for our further analysis because this shows the best performance. However, we compared all of our image analysis with D_{Mi} due to the above limitation of D_{LLS} in distinguishing the dependence of brightness on latitude from its dependence on geometry, and the slightly better performance of D_{Mi} at small phase angles. We confirm similar results on observed features that will be discussed in Section 4.1. This implies that either D_{LLS} or D_{Mi} can be used for the albedo analysis.

3.2. Radiative Transfer Model

We conduct RTM calculations using the software libRadtran (Mayer & Kylling 2005) version 2.0 released in 2015. We use the updated DISORT (Buras et al. 2011) with pseudospherical correction. A total of 101 layers are included in the RTM, from

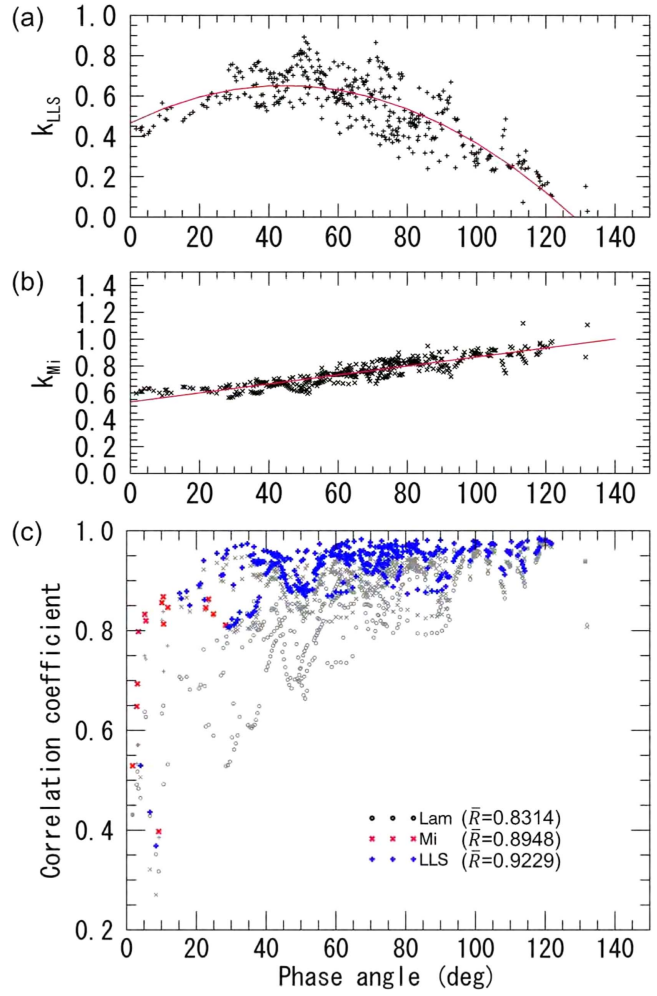

Figure 1. Coefficients determined for disk functions, and a comparison of photometric correction models at 283 nm. (a) $k_{LLS,283}(\alpha)$ (black cross) and a least-square fit of second order (red curve). (b) $k_{Mi,283}(\alpha)$ (black cross) and a linear least-square fit (red curve). (c) Results of correlation coefficients between observed images ($r_{F,283}$) and modeled images of the three disk functions (D_{283}). The least-square fits of $k_{LLS,283}(\alpha)$ and $k_{Mi,283}(\alpha)$ are used. The largest coefficient of the three is highlighted with a thick colored symbol for each image. Mean correlation coefficients ($\bar{R}$) are shown in the legend.

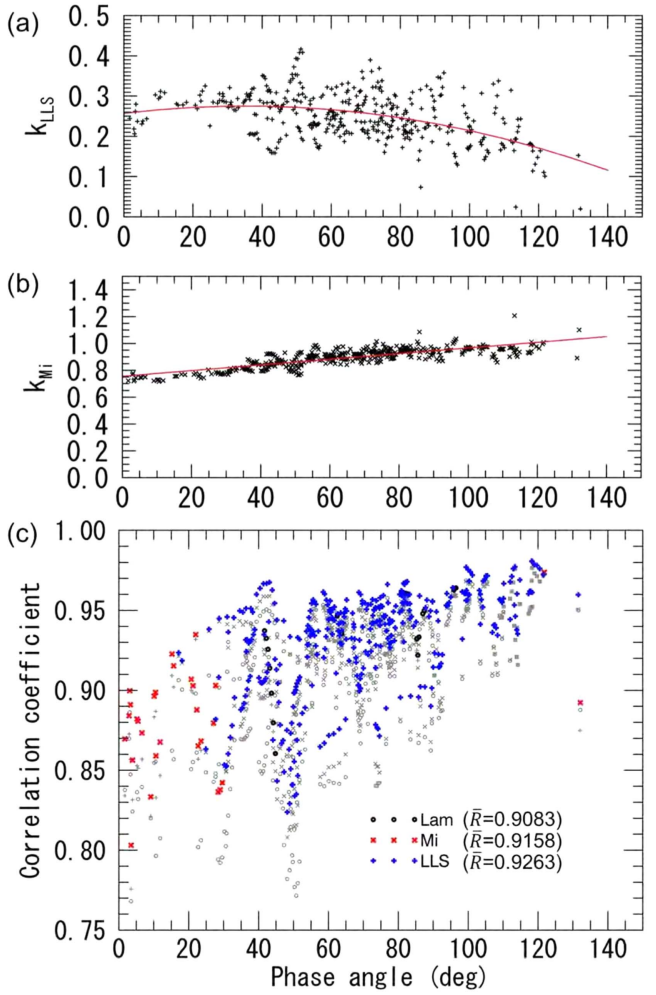

Figure 2. Coefficients determined for disk functions, and a comparison of photometric correction models at 365 nm. (a) $k_{LLS,365}(\alpha)$ (black cross) and a least-square fit of second order (red curve). (b) $k_{Mi,365}(\alpha)$ (black cross) and a linear least-square fit (red curve). (c) Results of correlation coefficients between observed images ($r_{F,365}$) and modeled images of the three disk functions (D_{365}). The least-square fits of $k_{LLS,365}(\alpha)$ and $k_{Mi,365}(\alpha)$ are used. The largest coefficient of the three is highlighted with a thick colored symbol for each image. Mean correlation coefficients ($\bar{R}$) are shown in the legend.

the surface to an altitude of 100 km. We calculate $r_{F,model}(\mu, \mu_0, \alpha)$ from the radiance at 100 km, and convert it to albedo as a function of phase angle, $A_{model}(\alpha)$,

$$A_{model}(\alpha) = \frac{r_{F,model}(\mu, \mu_0, \alpha)}{D_{LLS}(\mu, \mu_0, \alpha)}, \quad (11)$$

where D_{LLS} is the disk function determined using LLS (Equations (5), (7), (9)). The phase angle α is calculated from μ and μ_0, using the law of cosines for spherical triangles. μ_0 is fixed to 1.0 (= 0° solar zenith angle). μ has 62 grids, which are at intervals of 2° for emergence angles from 86° to 14°, and at smaller intervals of 0.3°–1.2° for emergence angles of less than 14°. This configuration is to simulate small phase angles properly.

3.2.1. Atmospheric Model

The atmospheric condition assumes the low latitudinal profiles of temperature, pressure, and atmospheric molecular number density described in Venus International Reference Atmosphere (Seiff et al. 1985). The atmospheric density profile is used to calculate Rayleigh scattering from CO_2 (Ityaksov et al. 2008).

A previous study using *Venus Express* data revealed decreasing cloud top altitudes from ~74 km at low latitudes to 63–69 km at a pole at 1.6 μm (Ignatiev et al. 2009), and a similar trend can be expected for the UV cloud top altitudes (see Figure 9 in Ignatiev et al. 2009 and Table 2 in Haus et al. 2015). Also the scale height of cloud aerosols can vary from <1 km to >6 km as determined in previous studies (Zasova et al. 2007; Lee et al. 2012). To take into account various cloud top structures, we decide to use an exponential function for the profile of the cloud extinction coefficient above 60 km (Lee et al. 2012). The vertical structure of the cloud top is described by a unity level of the optical depth at 365 nm and a scale height of cloud aerosols. In this study, we change the cloud top level from 66 to 74 km, and the scale height of cloud aerosols from 2 to 6 km, as free parameters. Below 60 km, the extinction coefficient of clouds is fixed to a constant

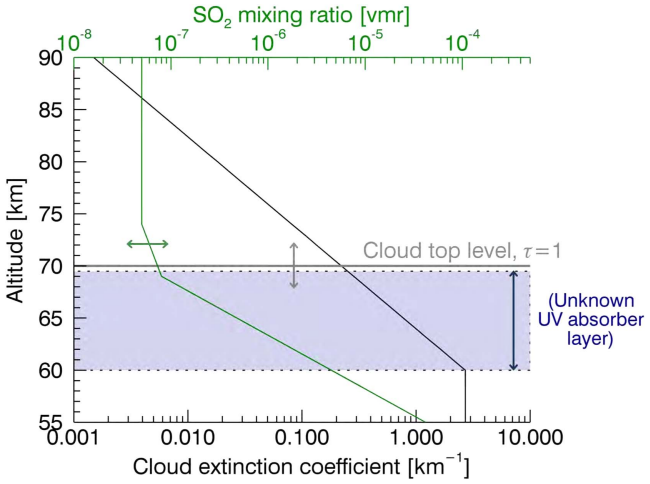

Figure 3. Configuration of the atmospheric model in this study. An example of a profile of the cloud extinction coefficient is shown for a cloud top altitude of 70 km and a scale height of cloud aerosols of 4 km. The unity level of optical depth is indicated with the gray line. A standard profile of SO_2 mixing ratio is shown as well (green). An example of the unknown UV absorber layer is shown with the blue shaded box (60–70 km). The arrows indicate the directions of flexibility of each parameter. See text for details.

(Figure 3), down to 48 km where is the cloud base (Seiff et al. 1985). Below the cloud base, no aerosols are assumed. An example of the vertical structure of the cloud top is shown in Figure 3.

Two modes of cloud aerosols are used in this study; small particles, so-called "mode 1," and larger particles, "mode 2." We introduce a ratio of extinction coefficients of these two modes, whose total extinction coefficient is equal to the above exponential profile of extinction coefficient. Scattering and absorption properties of modes 1 and 2 are calculated using Mie code (software: MIEV0, Wiscombe 1980). We use a complex refractive index equivalent to 75% sulfuric acid. The real part of the refractive index (n_r) has a temperature dependence (Palmer & Williams 1975; Hummel et al. 1988), and we use the value at 215 K (Hummel et al. 1988), which is close to the atmospheric temperature near the cloud top level. This is different from Petrova et al. (2015b), in which the authors modified n_r slightly as a free parameter. This study, however, uses a fixed $n_r(T = 215\,\mathrm{K})$, because this was used successfully for analysis of the cloud and upper haze aerosols using spectroscopic data from 0.67 to 1.7 μm (Luginin et al. 2016), implying that this should be a reasonable value. On the other hand, we vary the imaginary part of the refractive index (n_i) as a free parameter. This is selected among $n_i = 1.07 \times 10^{-8}$, 0.0002, 0.0005, and 0.0075, which were used in previous studies. The first value corresponds to that of pure sulfuric acid aerosol (Hummel et al. 1988). The second and third ($n_i = 0.0002$ and 0.0005) were used at 365 nm for the unknown UV absorber (Marov 1978; Petrova et al. 2015a). The last one ($n_i = 0.0075$) was used to fit observed UV spectra (Pollack et al. 1980), assuming that the unknown UV absorption extends to shorter wavelengths than 360 nm. A similar consideration was used in the more recent UV spectrometer study (SPICAV/*Venus Express*) (Marcq et al. 2011). We consider this possible absorption of the unknown UV absorber at 283 nm in this study as well. Therefore, we compare $n_i = 1.07 \times 10^{-8}$, 0.0002, 0.0005, and 0.0075 at 283 nm, and $n_i = 1.07 \times 10^{-8}$, 0.0002, and 0.0005 at 365 nm. The unknown UV absorber is known to exist in a thin layer near the cloud top level (Pollack et al. 1979; Esposito 1980), but Molaverdikhani et al. (2012) argued that it is difficult to reject a vertical extension of the unknown UV absorber above the cloud top altitude. We take into account such variability of the vertical location of the unknown UV absorber, assuming $n_i > 1.07 \times 10^{-8}$ over a range of altitudes, so the top and bottom altitudes of the unknown UV absorber layer are free parameters in this study (Figure 3).

Our initial size distributions of modes 1 and 2 were taken from Pollack et al. (1980). A log-normal size distribution function is used in the calculations with a geometric mean radius (r_0) of 0.15 μm and a geometric standard deviation (σ) of 1.91 for mode 1, and $r_0 = 1.05$ μm and $\sigma = 1.21$ for mode 2. We consider possible variations from the initial size distribution, and we prepared a database that is calculated using slightly different values from the above. Figure 4 shows the resulting phase function curves using the different size distributions at 283 and 365 nm. We find that the local minimum and maximum of the phase function at small phase angles can be easily controlled by the mode 2 size distribution. A larger r_0 causes a shift of the local maximum from a phase angle of 12° to 7° at 365 nm, and from 9° to 6° at 283 nm. Two local minima, one each side of a local maximum, move in a similar way. The effect of σ is different, as shown in Figure 4 (d): a larger variance in particle sizes reduces fluctuations of phase functions at small phase angles less than 20°. The size of mode 1 particles is relatively small compared to the wavelengths, so the phase function shows relatively slow changes over phase angles (Figures 4(a) and (b)). According to this result, we can understand that the most significant effect on a local maximum, the glory, would be caused by mode 2 aerosols. Moreover, we can estimate a mean particle size of mode 2 from the phase-angle location of a local maximum, and a variance from its shape. The effect of mode 1 would be a flattening of the phase curve.

The cross section for UV absorption by SO_2 is included in our model (Bogumil et al. 2003; Mayer & Kylling 2005). We assumed its vertical profile of mixing ratio to be as shown in Titov et al. (2007): 50 ppbv above 75 km, 80 ppbv at 70 km, increasing rapidly below that, and fixed at 200 ppmv below 53 km altitude (Figure 3). This profile has been multiplied by a certain factor, which is a free parameter in this study. The factor varies from zero to 10, equivalent to the variation in SO_2 abundance from 0 to 800 ppbv at the cloud top level.

4. Results

This section shows the results from the observed phase curves. We compare modeled phase curves under several assumed atmospheric conditions. We examine which atmospheric parameters affect the phase curve most, and control these effective parameters to fit the observation.

4.1. Observed Phase Curve

Using the albedo A (Equation (3)), we calculate the global mean value of each image. These mean albedos are then normalized to that at 30° phase angle, leaving the relative variation of albedo with phase angle. This allows us to

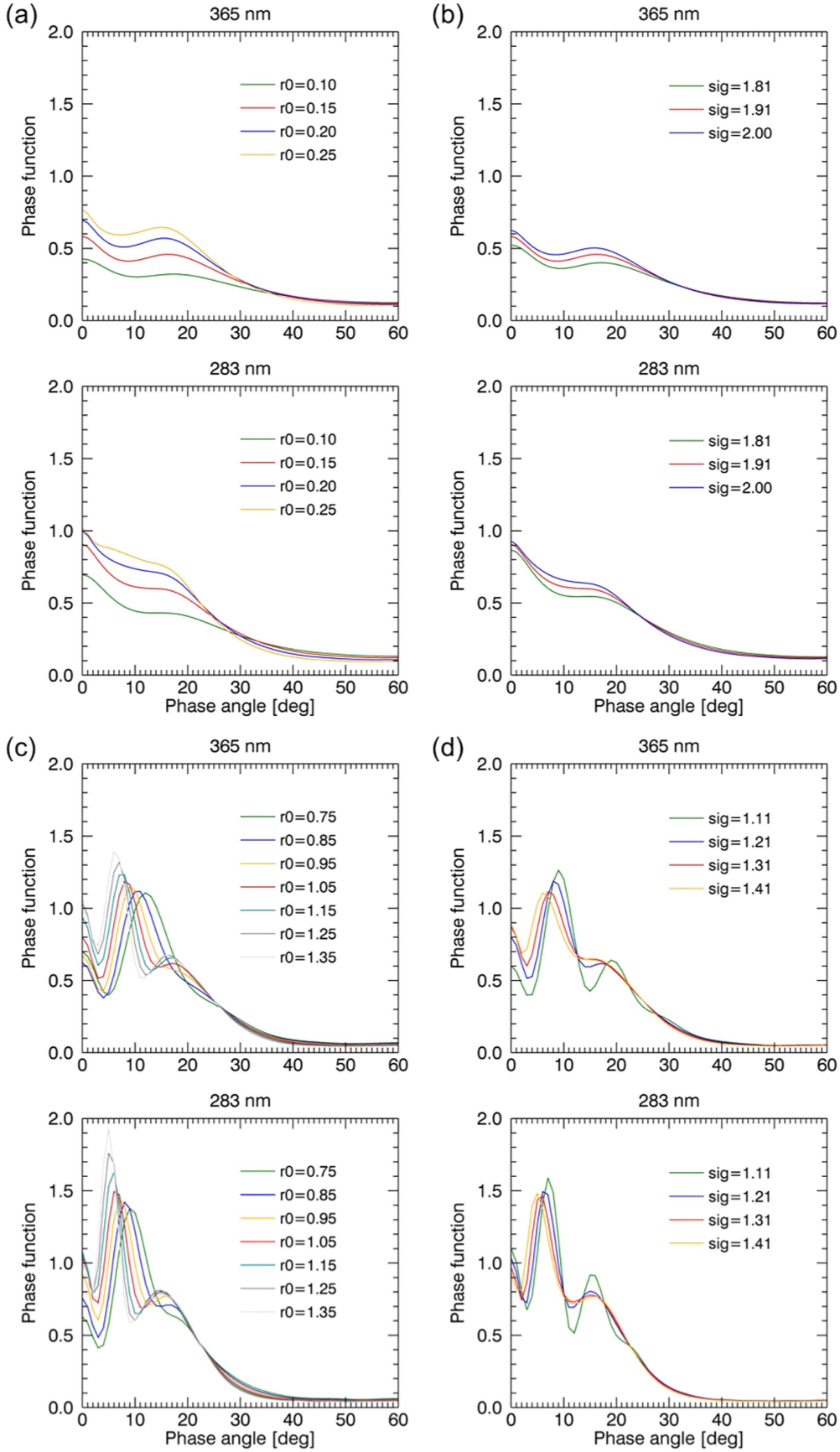

Figure 4. Phase functions of modes 1 and 2 at 283 and 365 nm (as marked) with various size distributions. (a) r_0 of the mode 1 size distribution from 0.10 to 0.25 μm. (b) σ of the mode 1 size distribution from 1.81 to 2.00. (c) r_0 of the mode 2 size distribution from 0.75 to 1.35 μm. (d) σ of the mode 2 size distribution from 1.11 to 1.41.

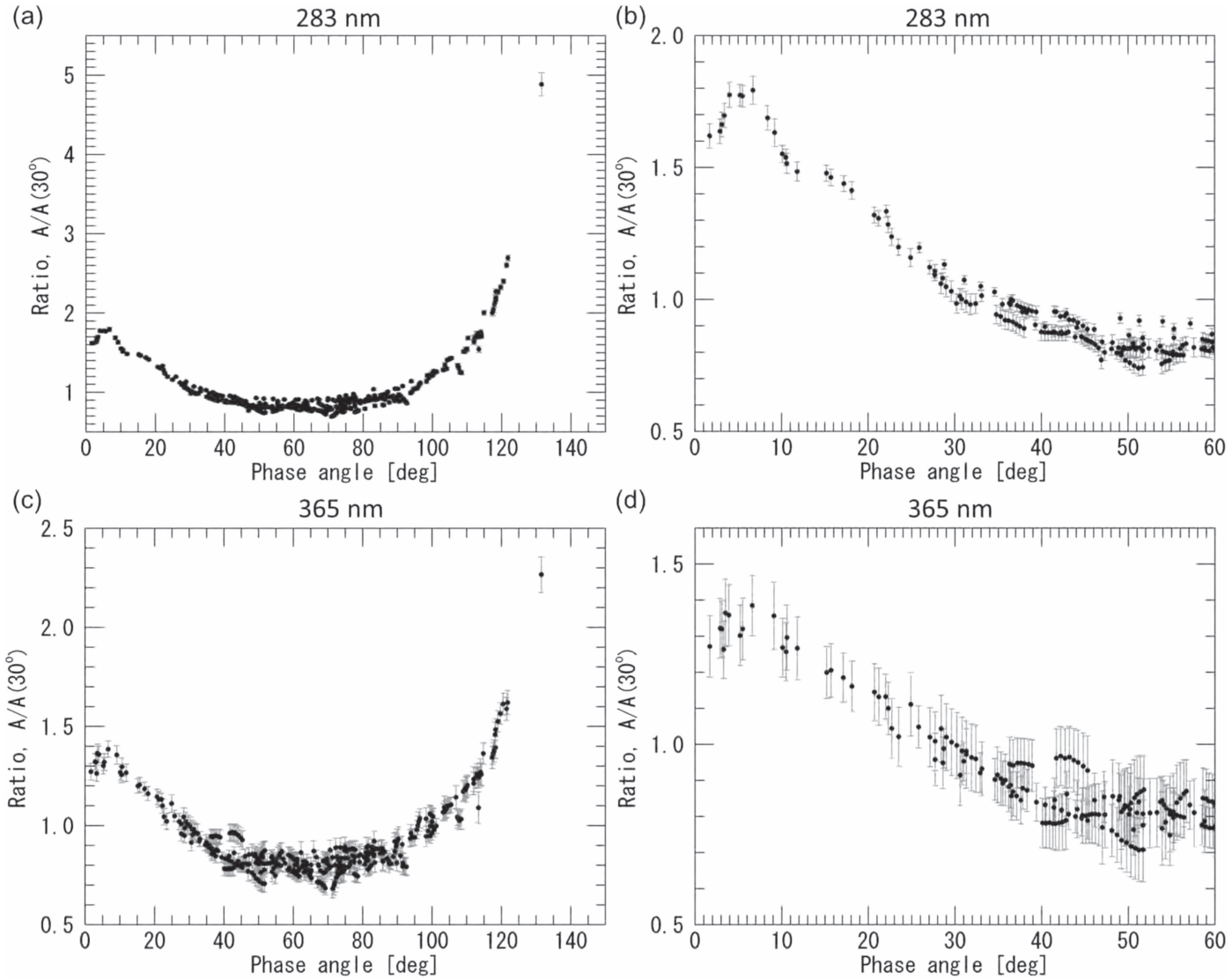

Figure 5. Observed phase-angle dependences of the relative global mean albedo. (a) All data at 283 nm. (b) Close-up of (a) for phase angles from 0° to 60°. (c) All data at 365 nm. (d) Close-up of (c) for phase angles from 0° to 60°.

understand the phase-angle dependence, regardless of an incomplete calibration of absolute radiance (Section 2.1). The variation of the resulting relative albedo with phase angle is shown in Figure 5. At small phase angles, glory features can be recognized ($\alpha < 10°$). Relative albedo gradually decreases, as phase angle increases up to 50°. The dependence becomes rather flat from 50° to 70° phase angles, and starts to increase above 70°. The drastic increase in relative albedo at large phase angles is consistent with strong forward scattering of aerosols. The phase curves at 283 and 365 nm show similar trends (Figures 5(a) and (c)), but the relative albedo at 283 nm has a stronger dependence on phase angle than that at 365 nm. Figures 5(b) and (d) magnify the areas of the glory feature. Error bars at 283 nm are smaller than those at 365 nm, because of smaller variations in albedo in one image at 283 nm.

There is a short-term temporal variation of relative albedo. For example, in Figure 5(d), a group of relative albedo points are higher than others in the 40°–45° range of phase angle. All of these are taken in one day. Similarly, data points aligned in phase angle can be found, and these are data taken during one day. This is caused by day-to-day changes of dark/bright features. The general shape of the phase curve including the glory seems to be less affected by this short-term variation, as there is no recognizable difference in the glory feature in the data acquired during *Akatsuki*'s three orbits in May.

4.2. Simulations at 283 nm

Figures 6(a) and (b) show the effects of cloud top structure on the phase-angle dependence of relative albedo at 283 nm. The mode 2 clouds are considered without any absorptions by the UV absorbers. The cloud top altitudes vary from 66 to 74 km, while the scale height of cloud aerosols is fixed at 4 km in Figure 6(a). Rayleigh scatterings above the cloud top affect the curves slightly. Using a fixed cloud top altitude at 70 km, the scale height of cloud aerosols is changed from 2 to 6 km in Figure 6(b), which shows no differences in the curves. In the following simulations, we use a fixed cloud top structure: a cloud top altitude of 70 km and a scale height of cloud aerosols of 4 km, which is the middle point of latitudinal variations in the cloud tops (Ignatiev et al. 2009).

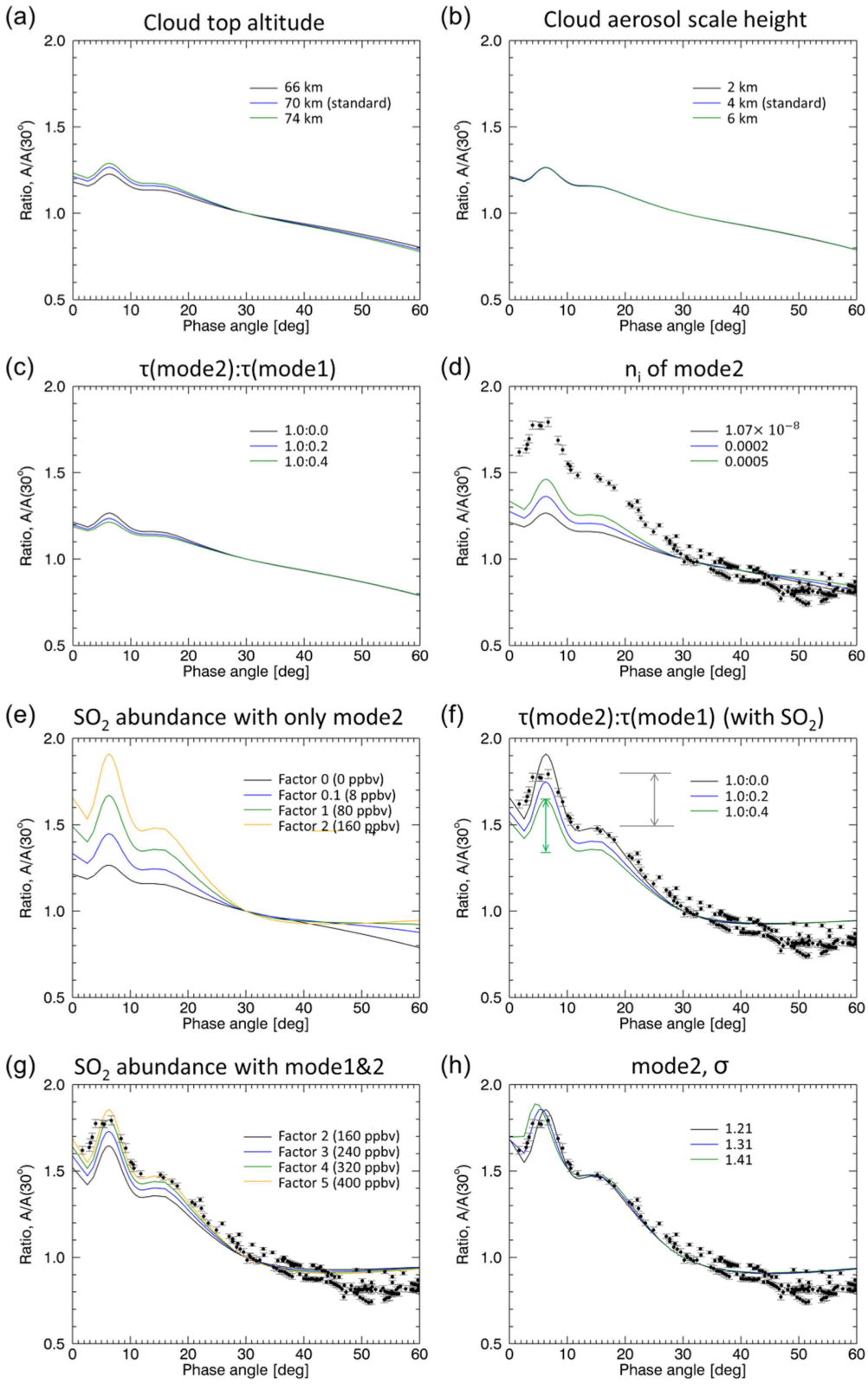

Figure 6. Results of the simulations (solid curves) and comparisons with the observation at 283 nm (filled circles). (a) Variation in cloud top altitude from 66 to 74 km. (b) Variation in scale height of cloud aerosols from 2 to 6 km. (c) Variation in the ratio of τ(mode 2) to τ(mode 1). (d) Various n_i of mode 2. (e) Profile of SO_2 mixing ratio increased/decreased from the standard by several factors. The corresponding volume mixing ratio at the cloud top level is shown in brackets. (f) Various ratios of τ(mode 2) to τ(mode 1) under the profile of SO_2 mixing ratio increased by a factor of 2; 160 ppbv at the cloud top level. (g) Profile of SO_2 mixing ratio increased/decreased from the standard by several factors, using τ(mode 2):τ(mode 1) = 1.0:0.4. Corresponding volume mixing ratios at the cloud top level are shown in brackets. (h) Various σ for the mode 2 size distribution. This assumes τ(mode 2):τ(mode 1) = 1.0:0.4 and the profile of SO_2 mixing ratio increased by a factor of 5; 400 ppbv at the cloud top level.

Figure 6(c) shows the effects on the phase curve of an increased mode 1 portion in the total cloud opacity. The ratio of the extinction coefficient of mode 2 to that of mode 1, τ (mode 2):τ(mode 1), is 1.0:0.2 in Figures 3-4(a) of Ragent et al. (1985). We compare results using ratios of 1.0:0.0, 1.0:0.2, and 1.0:0.4. A weak signature of the flattening effect of mode 1 can be found, consistent with our expectation from Figure 4.

The absorption of the unknown UV absorber at 283 nm is not yet confirmed, so first we compare results using $n_i = 0.0002$ and 0.0005, the same values used at 365 nm. Figure 6(d) shows the resulting phase curves. Note that we assume that the unknown UV absorber layer extends from 60 to 100 km altitude, i.e., the entire upper cloud layer, as a possible condition suggested in Molaverdikhani et al. (2012). This condition maximizes the absorption of the unknown UV absorber. The peak of the glory becomes clearer with larger n_i values, corresponding to conditions of greater absorption. However, we notice a still considerable difference between the simulated curves and the observed feature, whose relative albedo reaches 1.8 at 6° phase angle.

Figure 6(e) presents the effects of SO_2 absorption on relative albedo, but without the unknown UV absorber. The standard profile of SO_2 mixing ratio is multiplied by factors from 0 to 2. This is equal to a range of SO_2 abundance from 0 to 160 ppbv at the cloud top level. The result shows a more significant influence on the phase curve than those of cloud top structures, n_i modifications up to 0.0005, and the ratio of mode 2 to mode 1.

After comparing a number of cases, we find that it is difficult to get one single solution to explain the observed phase curve, e.g., assumptions on the unknown UV absorber lead to different solutions. Here, we describe the process used to find solutions that explain the observed features successfully. Diverse conclusions on atmospheric conditions could be reached under the following three assumptions on the absorptions of the unknown UV absorber at 283 nm.

Assumption 1: No absorption

Considering the observed relative albedo, the unknown UV absorber is not a necessary parameter at 283 nm, unlike when fitting the UV spectrum (Pollack et al. 1980; Marcq et al. 2011). SO_2 absorption alone can produce a significant effect on the relative albedo as shown in Figure 6(e). The black curve in Figure 6(f) is comparable to the observation when SO_2 abundance is increased by a factor of 2 (=160 ppbv at 70 km).

The peak of the glory is rather sharp in the above model result. This sharp peak can be smoothed with an increased mode 1 portion in the clouds. When τ(mode 2):τ(mode 1) = 1.0:0.4 (green curve in Figure 6(f)), the simulated glory peak can be close to the observation, as shown by the green and gray vertical arrows, which have the same length. This condition, however, requires a greater SO_2 abundance to fit the observed relative albedo, i.e., the yellow curve in Figure 6(g) that assumes an SO_2 abundance increased by a factor of 5. This is equal to 400 ppbv of SO_2 at the cloud top level, about the maximum value of past observations (Marcq et al. 2013).

The yellow curve of Figure 6(g) generally fits the observation well, except for the 0°–6° range of phase angle. This discrepancy can be removed using a larger variance of mode 2 (Figure 4(d)). We compare the results using different variances from 1.21 to 1.41 for mode 2, and successfully fit the observation using $\sigma = 1.31$ (Figure 6(h)). Hereafter, this size distribution is used for mode 2 at 283 nm, and we find no reason to reject this variance, owing to a successful fit of the observed glory.

Assumption 2: $n_i \leqslant 0.0005$

Inclusion of the unknown UV absorber at 283 nm can reduce the required SO_2 abundance slightly. Figure 7(a) shows a comparison of n_i for the unknown UV absorber (60–100 km). We compare different top levels of the unknown UV absorber layer in Figure 7(b), assuming $n_i = 0.0005$. This shows a negligible effect on the relative albedo, implying that the top level of the unknown UV absorber layer is difficult to determine under assumption 2. For simplicity, we assume the unknown UV absorber layer to lie in the altitude range 60–70 km, and change the ratio of extinction coefficients of mode 2 and mode 1, and SO_2 abundances in Figures 7(c) and (d), respectively. We find a best fit as shown by the blue curve in Figure 7(d), with mode 2 dominating clouds and a 120 ppbv SO_2 abundance at the cloud top level.

Assumption 3: $n_i = 0.0075$

Under this assumption of large n_i, the phase-angle dependence of relative albedo can be increased drastically as shown by the green curve in Figure 8(a). This assumes mode 2 dominating clouds and the standard profile of SO_2 mixing ratio. In addition, the vertical location of the unknown UV absorber layer becomes another important factor in the phase-angle dependence. Figure 8(b) shows that the most effective case is when the unknown UV absorber exists below the cloud top level (black curve). Then below the cloud top level, depths of less than 10 km for the unknown UV absorber layer are also compared, although this is not shown as a figure. This absorption effect of the unknown UV absorber can be maintained for layers as shallow as 2 km, as long as the layer is located right below the cloud top altitude. If the bottom of the unknown UV absorber layer exists above the cloud top level, then its absorption is not effective enough (blue and green curves in Figure 8(b)). On the other hand, if the unknown UV absorber is well mixed in the clouds from 60 to 100 km altitude, then this causes a too strong absorption, and backward scattering is suppressed (yellow curve in Figure 8(b)). This case would require a smaller r_0 than the current value ($r_0 = 1.05\,\mu$m) to fit the observed glory by shifting the locations of the local maximum and minima to larger phase angles (see Figure 4(c)).

The standard profile of SO_2 mixing ratio can be sufficient to fit the observation under assumption 3 (Figures 8(a) and (b)). But we can reduce the too sharp peak of the simulated glory by increasing the portion of mode 1 (Figure 8(c)). Or, we could fit the observation reasonably well assuming that the unknown UV absorber layer exists above the cloud top level (70–75 km). This case requires the SO_2 mixing ratio to be increased by a factor of 1.5–2.0 to fit the observation (Figure 8(d)).

4.3. Simulations at 365 nm

A similar process is repeated at 365 nm as is done at 283 nm. We start with the initial properties of aerosols (Pollack et al. 1980), so return to $\sigma = 1.21$ for mode 2. First, the cloud top structures are compared. Without any assumption about the UV absorber, the cloud top altitude is changed from 66 to 74 km with a 4 km scale height of cloud aerosols (Figure 9(a)), and the scale height of cloud aerosols is changed from 2 to 6 km with a cloud top altitude of 70 km (Figure 9(b)). These results show negligible effects of the cloud top structure on the relative albedo at 365 nm. Differences in relative albedo due to

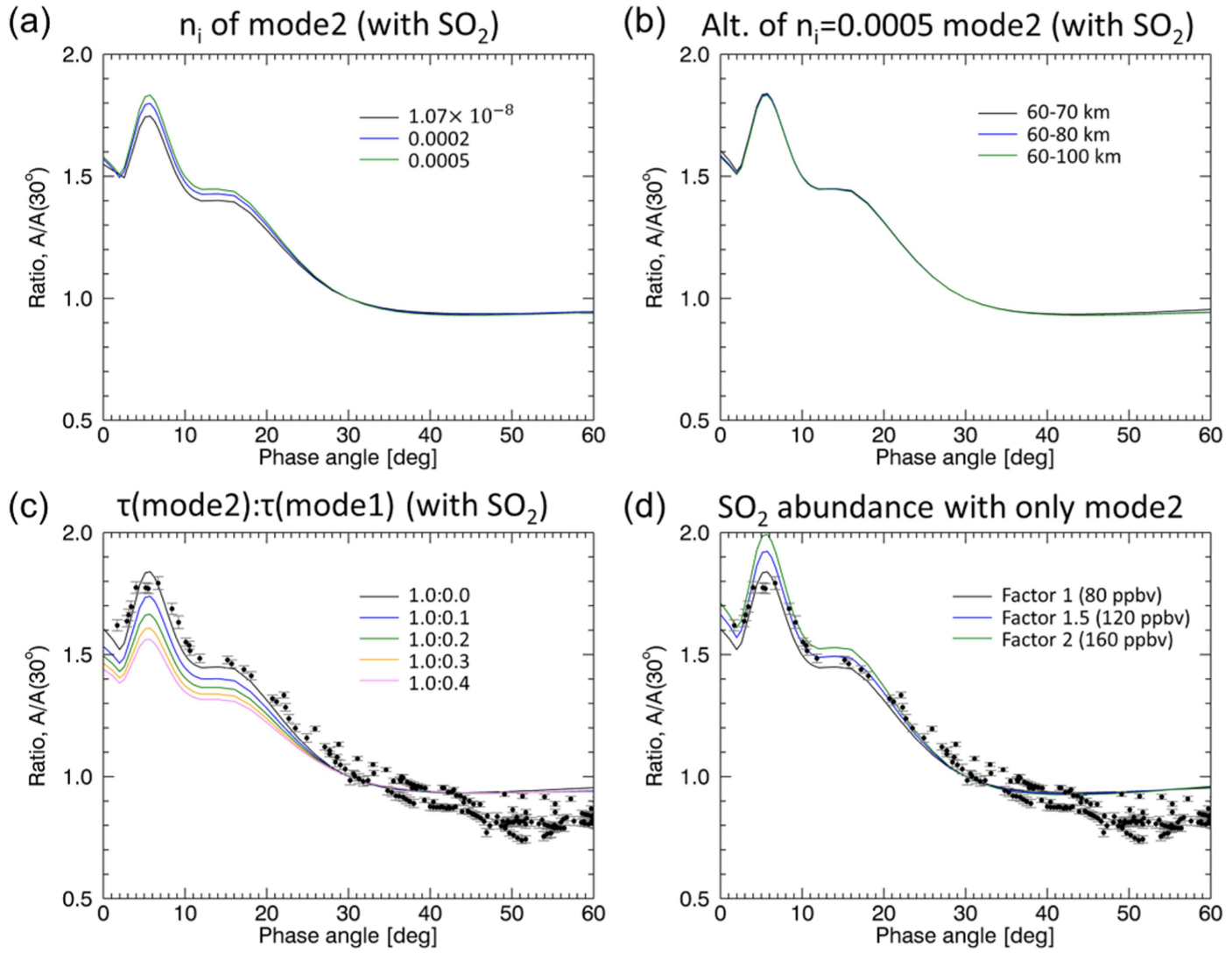

Figure 7. Results of the simulations with assumption 2 (solid curves) and their comparisons to the observation at 283 nm (filled circles). All cases use $\sigma = 1.31$ for mode 2. The standard profile of SO_2 mixing ratio is used for cases (a)–(c). (a) Various n_i for mode 2 from 60 to 100 km altitude. (b) Different vertical ranges of the unknown UV absorber layer ($n_i = 0.0005$ for mode 2). (c) Various ratios τ(mode 2):τ(mode 1). (d) Profiles of SO_2 mixing ratio increased from the standard by several factors. Corresponding volume mixing ratios at the cloud top level are shown in brackets. This assumes τ(mode 2):τ(mode 1) = 1.0:0.0 and the unknown UV absorber layer is in the altitude range 60–70 km ($n_i = 0.0005$).

different cloud top altitudes are smaller at 365 nm than at 283 nm, as Rayleigh scattering is weaker at 365 nm (Figures 6(a) and 9(a)).

The flattening effect of mode 1 can be seen in Figure 9(c); if we increase the portion of mode 1, then the results show a reduced peak of the glory. Using the cloud dominated by mode 2, we change n_i from 1.07×10^{-8} to 0.0002 and 0.0005 between 60 and 100 km altitudes. $n_i = 0.0005$ shows the strongest influence on the phase-angle dependence of relative albedo. In addition, there are weak absorptions of SO_2 up to 395 nm wavelength (Bogumil et al. 2003), which can be another parameter to affect relative albedo. This has been tested by increasing SO_2 abundance up to 10 times the standard condition, which is equal to 800 ppbv at the cloud top level. Figure 9(e) shows the negligible effect of SO_2 absorption on a phase curve at 365 nm, implying that it is safe to assume zero SO_2 abundance at 365 nm in the following calculations.

Under the assumption of an unknown UV absorber of $n_i = 0.0005$ for mode 2 in the altitude range 60–100 km, we again compare the flattening effect of mode 1 in Figure 9(f). The results show that the clouds dominated by mode 2 are preferable to fit the observation. The result is the same if only mode 2 is incorporated with the unknown UV absorber (Figure 9(f)), or if both mode 1 and mode 2 are incorporated (not shown as a figure).

The vertical extent of the unknown UV absorber layer is compared in Figure 9(g). This assumes clouds dominated by mode 2, and $n_i = 0.0005$ in the unknown UV absorber layer. Interestingly, the difference from the observation is rather small as long as the UV absorber exists below the cloud top level, but it becomes large when the unknown UV absorber exists above it (yellow curve in Figure 9(g)). We therefore conclude that the unknown UV absorber should exist below the cloud top level. However, we cannot estimate the top level of the unknown UV absorber layer, because simulated relative albedo is not

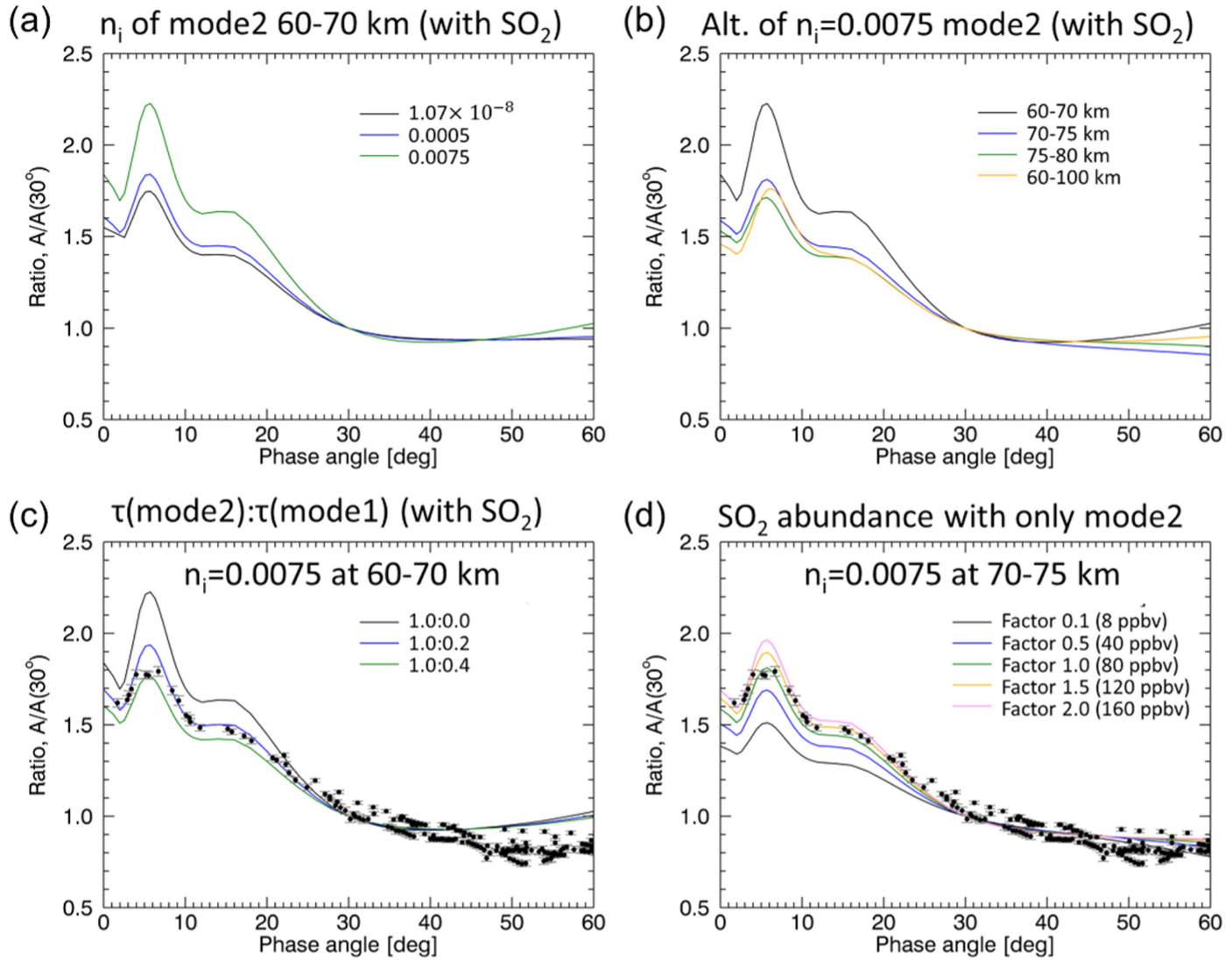

Figure 8. Results of the simulations with assumption 3 (solid curves) and their comparisons to the observation at 283 nm (filled circles). All cases use $\sigma = 1.31$ for mode 2. The standard profile of SO_2 mixing ratio is used from (a) to (c). (a) Various n_i for mode 2 used in the altitude range 60–70 km. (b) Different vertical ranges of the unknown UV absorber layer ($n_i = 0.0075$ for mode 2). (c) Various ratios of τ(mode 2) to τ(mode 1). Mode 1's n_i follows that of 75% pure sulfuric acid, and $n_i = 0.0075$ for mode 2 is used in the altitude range 60–70 km. (d) Profiles of SO_2 mixing ratio increased/decreased from the standard by several factors. Corresponding volume mixing ratios at the cloud top level are shown in brackets. This assumes only mode 2 clouds and that the unknown UV absorber layer is in the altitude range 70–75 km ($n_i = 0.0075$).

sensitive enough to distinguish the effects of various top levels, between 70 and 100 km.

Differences between the observation and simulations at small phase angles of less than 10° can be reduced when we increase σ to 1.31 for mode 2 in Figure 9(h). The error bars of the observation are quite large, so it is ambiguous to find a solution. This property of size distribution, however, is well consistent with the value determined at 283 nm.

5. Discussion

The phase-angle dependence of relative albedo is analyzed in this study. A number of assumptions on atmospheric conditions are compared in our model calculations, and we find several possible solutions that explain the observation (Figure 10 and Table 1). A common condition is $\sigma = 1.31$ for mode 2. This value can be converted to effective radius ($r_{\rm eff}$) and effective variance ($v_{\rm eff}$) using the equations below:

$$r_{\rm eff} = r_0 \exp\left(\frac{5}{2}\ln^2\sigma\right), \quad (12)$$

$$v_{\rm eff} = \exp(\ln^2\sigma) - 1. \quad (13)$$

Corresponding values are $r_{\rm eff} = 1.26\,\mu$m and $v_{\rm eff} = 0.076$. These are a little different from our initial values, $r_{\rm eff} = 1.15\,\mu$m and $v_{\rm eff} = 0.037$, taken from Pollack et al. (1980). However, this result is rather consistent with the analysis of Petrova et al. (2015a, 2015b) on the glory at 365 and 965 nm. Those authors found $r_{\rm eff} = 1.4$–$1.6\,\mu$m at low latitudes, and $r_{\rm eff} = 0.8$–$1.2\,\mu$m at high latitudes, while $v_{\rm eff} = 0.07$. In the UVI images, the area of low latitude from 30° S to 30° N occupies over 60% of the total valid pixels. So we consider that large particles at low latitudes can affect the global mean condition in this study. We find a similar value of

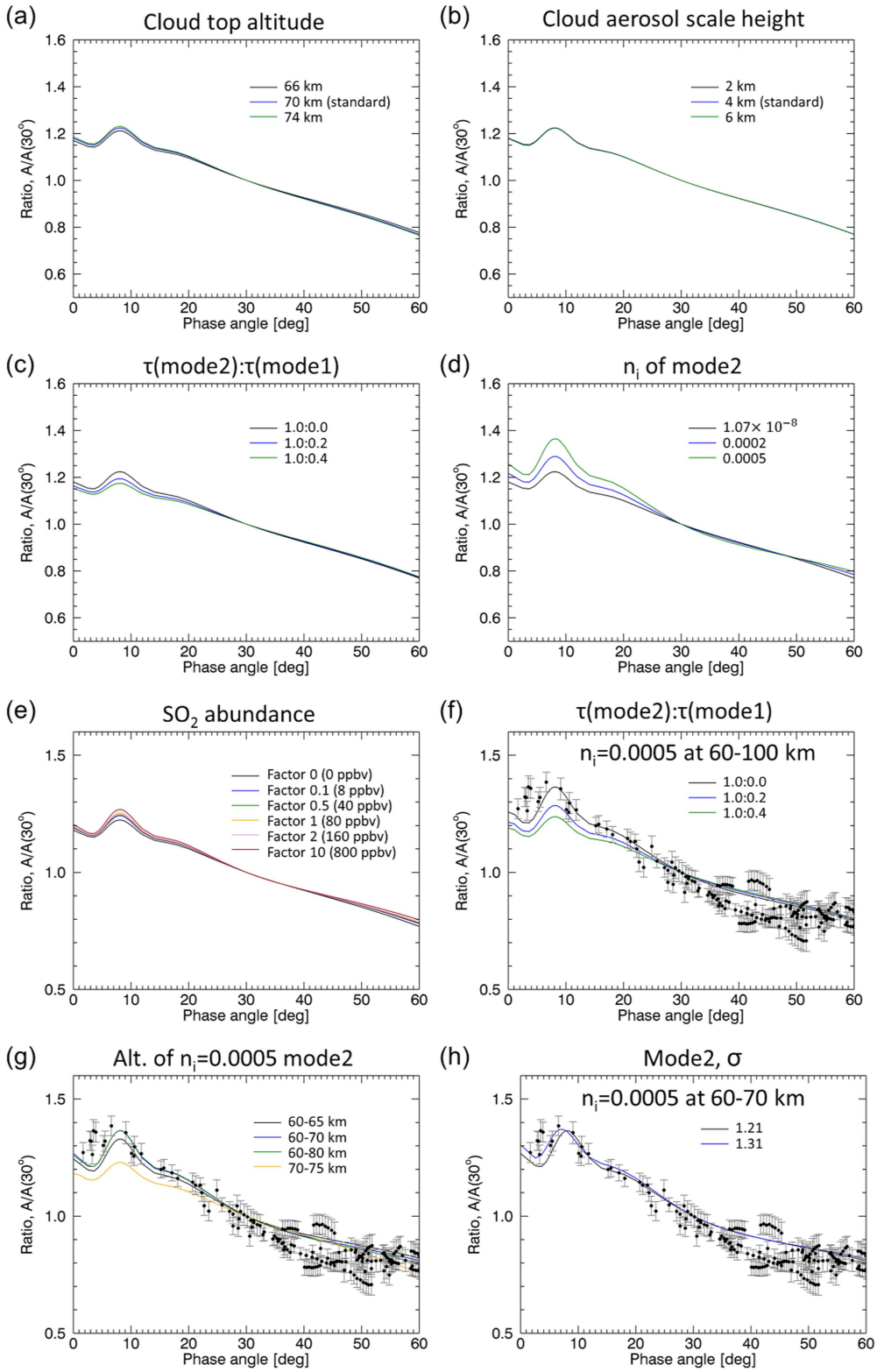

Figure 9. Results of the simulations (solid curves) and their comparisons to the observation at 365 nm (filled circles). (a) Variation in cloud top altitude from 66 to 74 km. (b) Variation in scale height of cloud aerosols from 2 to 6 km. (c) Various ratios of τ(mode 2) to τ(mode 1). (d) Different n_i of mode 2 in the altitude range 60–100 km. (e) Profile of SO_2 mixing ratio increased/decreased from the standard by several factors. Corresponding volume mixing ratios at the cloud top level are shown in brackets. (f) Various ratio of τ(mode 2):τ(mode 1). This assumes the unknown UV absorber layer to be in the altitude range 60–100 km ($n_i = 0.0005$). (g) Different vertical ranges of the unknown UV absorber layer ($n_i = 0.0005$) (blue and green curves are identical). (h) Various σ of mode 2. The unknown UV absorber layer is assumed to be in the altitude range 60–70 km ($n_i = 0.0005$).

effective variance of mode 2 in other previous studies, by Satoh et al. (2015) and Rossi et al. (2015), which could simulate observations successfully using $r_{\rm eff} = 1$–$1.2\ \mu$m and $v_{\rm eff} = 0.07$. García Muñoz et al. (2014) simulated observations using $r_{\rm eff} = 1\ \mu$m and $v_{\rm eff} = 0.037$ for mode 2, which are smaller than this study; they used data taken in 1999–2004,

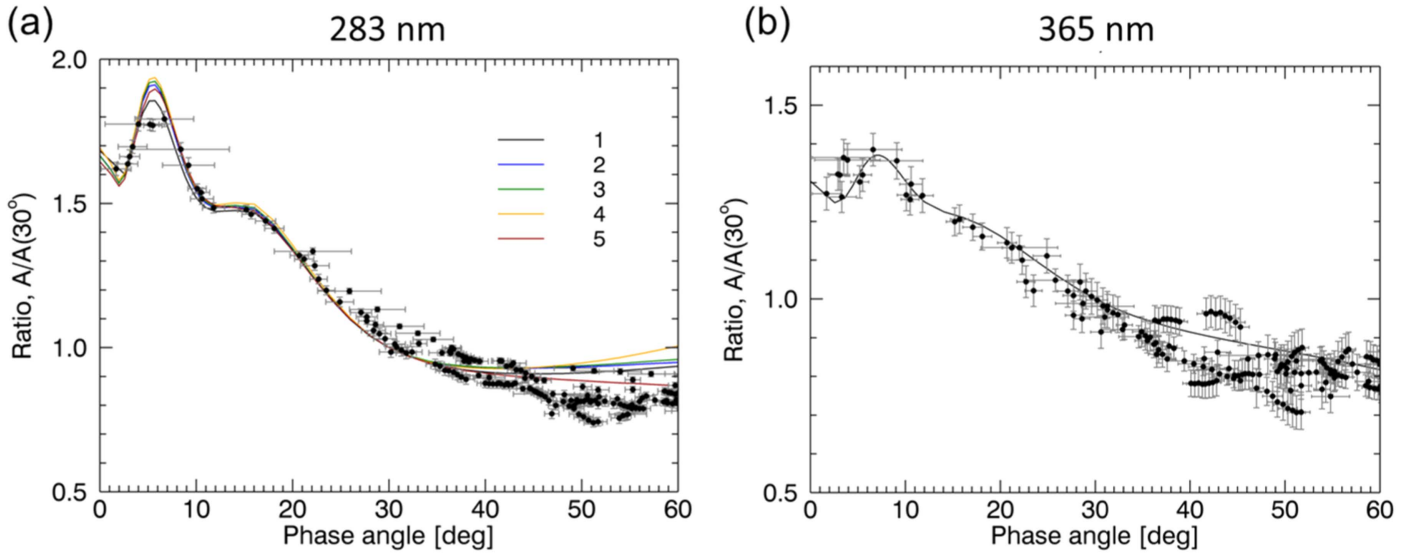

Figure 10. Comparison of best-fit models and observations at (a) 283 nm and (b) 365 nm. The different conditions of each curve (1–5) are described in Table 1. Horizontal error bars indicate the range of phase angle for each image.

Table 1
Summary of Best-fit Simulation Conditions in Figure 10

Wavelength (nm)	283					365
Index of curve	1	2	3	4	5	
SO_2 at 70 km (ppbv)	400	160	120	80	120–160	None
τ(mode 2):τ(mode 1)	1.0:0.4	1.0:0.0	1.0:0.0	1.0:0.2	1.0:0.2	1.0:0.0
Unknown UV absorber layer (km)	None	None	60–70[a]	60–70	70–75	60–70[a]
n_i of mode 2[b]	1.07×10^{-8}	1.07×10^{-8}	0.0005	0.0075	0.0075	0.0005
$r_{\rm eff}$ (r_0) of mode 2 (μm)	1.26 (1.05)					
$v_{\rm eff}$ (σ) of mode 2	0.076 (1.31)					
Cloud top structure	cloud top at 70 km, and scale height of cloud aerosols of 4 km					

Notes.
[a] The top level of the unknown UV absorber layer can be between 70 and 100 km.
[b] n_i is applied in the unknown UV absorber layer, and $n_i = 1.07 \times 10^{-8}$ is used for all other altitudes.

12–17 years before *Akatsuki*'s observation. Therefore, it would not be appropriate to make a direct comparison with this study.

We suggest that absorptions by the UV absorbers are necessary to explain the observed phase-angle dependence of relative albedo. The SO_2 mixing ratio at 70 km can be 80–400 ppbv, depending on whether we include or exclude the absorption of the unknown UV absorber at 283 nm. This also depends on the ratio of mode 1 particles to mode 2 and the vertical location of the unknown UV absorber layer. The result at 365 nm provides a clue to reduce the possible solutions, as the following two conditions are preferred. One is that the bottom level of the unknown UV absorber layer should be below the cloud top level. The other is that mode 2 dominates the clouds. These can be satisfied at 283 nm using the conditions of curves 2 and 3 in Figure 10(a) and Table 1. These require 120–160 ppbv SO_2 abundance near the cloud top level. This is the most preferable solution in this study.

We therefore use the condition of curve 3 in Figure 10 and Table 1, one of the above preferred solutions, and compare the effects of r_0 and σ of the size distribution of mode 2 at 283 and 365 nm (Figure 11). We calculate differences of relative albedo between simulations (S) and the observation (O) with phase angle (α) as

$$\chi^2 = \sum_{\alpha} \frac{(O_\alpha - S_\alpha)^2}{S_\alpha}. \quad (14)$$

We calculate χ^2 at phase angles less than 30°, where the glory features are prominent. In total, 34 elements are used for the phase angle. The results for χ^2 are shown in Figures 11(e) and (f). We find the consistency that the best fit can be achieved using $\sigma = 1.31$ and $r_0 = 1.05\ \mu$m for mode 2 at 283 nm. We do not interpret that at 365 nm, because of the observed large error bars.

We understand, however, that our results are based on limited freedom of parameters. If one allows more free parameters, such as various n_r and n_i, a finer vertical range of the unknown UV absorber, various profiles of SO_2 mixing ratio, and so on, then there will be more possible combinations that can fit the observation. In future, we aim to compare our results with observations from ground-based and space-based spectrometers that can determine SO_2 abundance at the cloud

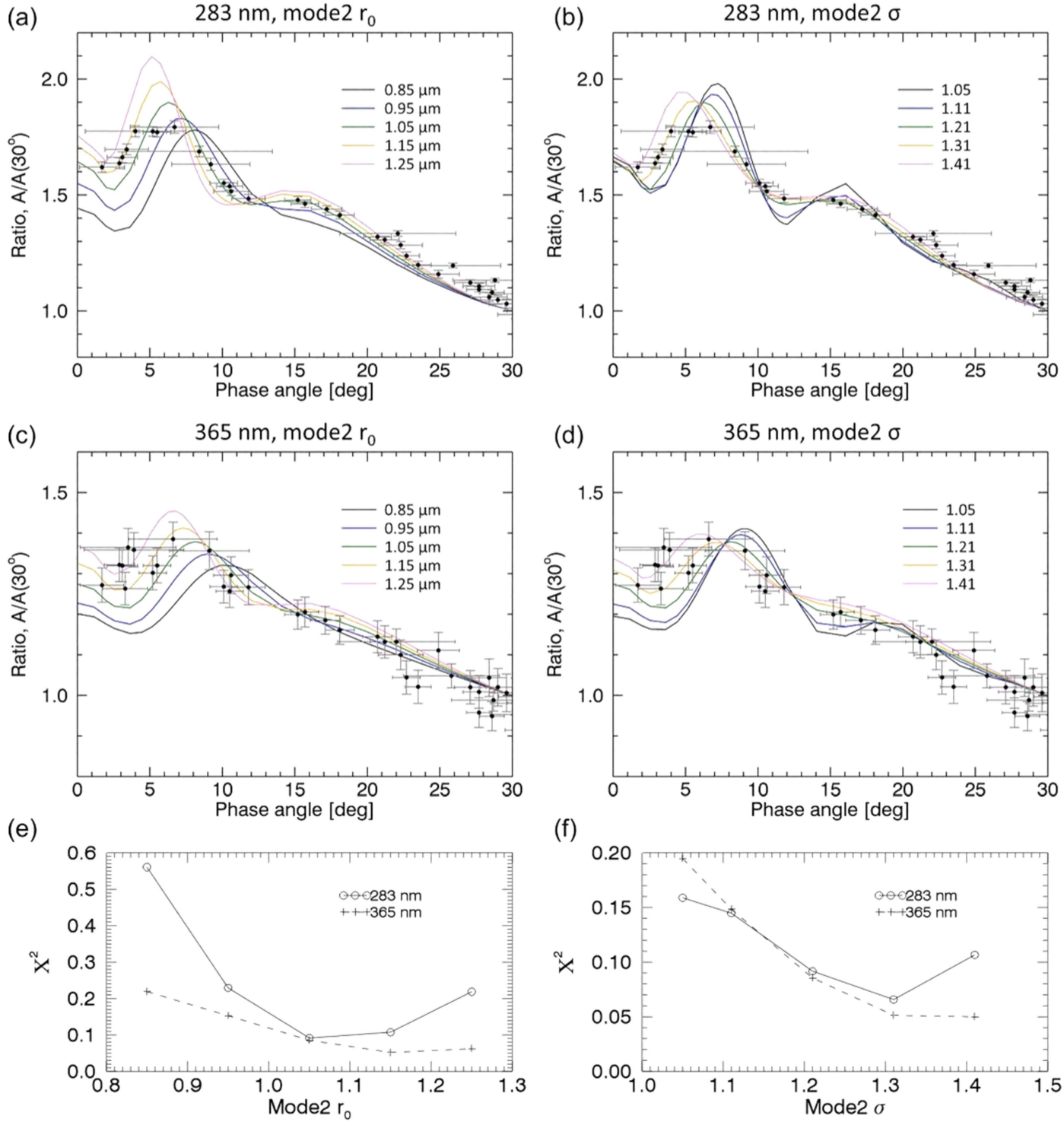

Figure 11. Comparison of mode 2's size distribution using condition 3 in Table 1. (a) Various r_0 at 283 nm, from 0.85 to 1.25 μm. (b) Various σ at 283 nm, from 1.05 to 1.41. (c) Various r_0 at 365 nm. (d) Various σ at 365 nm. (e) χ^2 for various r_0. (f) χ^2 for various σ. See text for details.

top level (Encrenaz et al. 2013; Jessup et al. 2015). This will allow us to recognize atmospheric conditions that support a specific SO_2 abundance. In addition, we will use absolute albedo for our future analysis, which will be better for estimating the abundances of UV absorbers.

Due to the small apparent diameter of Venus in the selected UVI images, we are not able to show a complete glory feature in a single image, as done in Markiewicz et al. (2014). Alternatively, we align a sequence of images at 283 nm acquired on 2016 May 5–6 with phase angle in Figure 12. These several images present the phase-angle dependence of albedo, from its maximum between phase angles of 4° and 8° to a darker condition at 22°. We show that this observed variation in albedo with phase angle can be explained by the

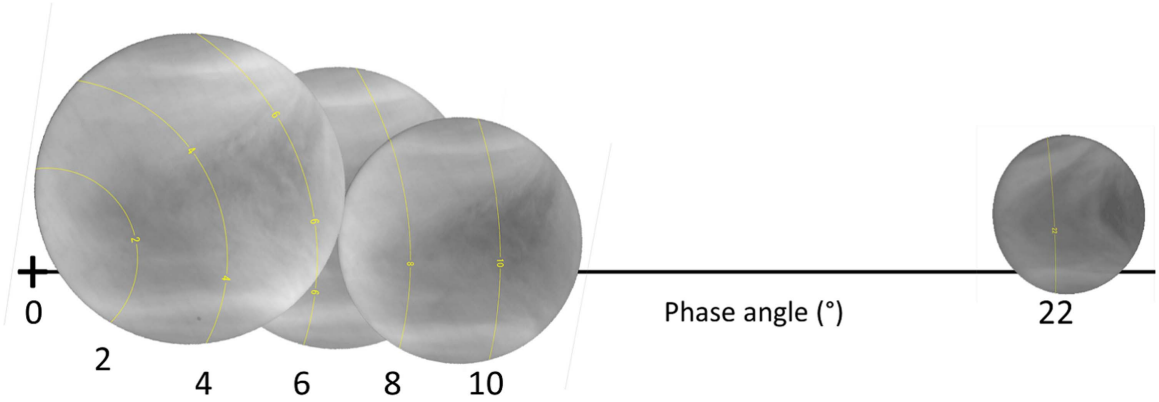

Figure 12. 283 nm images taken at 2016 May 5 15:14, 10:14, and 12:14, and May 6 14:00 in UTC, from right to left. Albedo is scaled to the same range from 0 (black) to 0.3 (white) for all images, and the nightsides are removed. Yellow circles and numbers indicate phase angles. The north of Venus is toward the bottom. A black dot near phase angle 4° and faint diagonal stripes are artifacts.

phase-angle dependence of the scattering and absorption properties of the same atmosphere, rather than a short-term variation of absorptions.

6. Summary

We investigate 283 and 365 nm images taken by UVI/*Akatsuki*. The analyzed data were acquired from 2015 December to 2016 August, and we focus on the May data analysis that reveals the glory feature. Photometric correction has been done in data processing, and we present the observed phase curves of relative albedo in the 283 and 365 nm channels. Both phase curves show strong forward and backward scatterings, while that at 283 nm has a more prominent glory feature than that at 365 nm. We explain the phase-angle locations of the local maximum and minima of the observed glory with 75% sulfuric acid cloud aerosols of $r_{\rm eff} = 1.26\ \mu$m and $v_{\rm eff} = 0.076$ (mode 2).

We suggest that the strong phase-angle dependence at 283 nm is caused by the mode 2 scatterings and SO_2 absorptions, but the required SO_2 abundance can vary depending on assumptions made about the unknown UV absorber at 283 nm. We explore possible combinations of absorptions and scatterings near the cloud top level: absorptions of SO_2 and the unknown UV absorber, the vertical location of this absorber, and the inclusion of mode 1 (small particles). Several combinations can fit the observation reasonably well (Figure 10 and Table 1), and our most preferred combinations are an SO_2 abundance of 120–160 ppbv at the cloud top level, clouds dominated by mode 2, and the bottom level of the unknown UV absorber layer located below the cloud top altitude. Simulations using these conditions can explain the observations in both channels. However, we are aware of other possible solutions, and further studies are required. We also plan to use an absolute albedo in a future study to determine the absorption with better precision.

The authors thank the *Akatsuki* team for management of satellite observations and data pipeline. This work is supported by the *Akatsuki* project. T. M. Sato was supported by JSPS KAKENHI Grant Number JP16K17816.

References

Bogumil, K., Orphal, J., Homann, T., et al. 2003, J. Photochem. Photobiol. A, 157, 167
Buras, R., Dowling, T., & Emde, C. 2011, JQSRT, 112, 2028
Buratti, B., & Veverka, J. 1983, Icar, 55, 93
Chance, K., & Kurucz, R. L. 2010, JQSRT, 111, 1289
Encrenaz, T., Greathouse, T. K., Richter, M. J., et al. 2013, A&A, 559, A65
Esposito, L. W. 1980, JGRA, 85, 8151
Frandsen, B. N., Wennberg, P. O., & Kjaergaard, H. G. 2016, GeoRL, 43, 11
García Muñoz, A., Pérez-Hoyos, S., & Sánchez-Lavega, A. 2014, A&A, 566, L1
Hapke, B. 2012, Theory of Reflectance and Emittance Spectroscopy (2nd ed.; Cambridge: Cambridge Univ. Press)
Haus, R., Kappel, D., & Arnold, G. 2015, P&SS, 117, 262
Hummel, J. R., Shettle, E. P., & Longtin, D. R. 1988, A New Background Stratospheric Aerosol Model for Use in Atmospheric Radiation Models, Tech. Rep. (Fort Belvoir, VA: Defense Technical Information Center), http://www.dtic.mil/docs/citations/ADA210110
Ignatiev, N. I., Titov, D. V., Piccioni, G., et al. 2009, JGRE, 114, E00B43
Ityaksov, D., Linnartz, H., & Ubachs, W. 2008, CPL, 462, 31
Jessup, K. L., Marcq, E., Mills, F., et al. 2015, Icar, 258, 309
Krasnopolsky, V. A. 2017, Icar, 286, 134
Lee, Y. J., Imamura, T., Schröder, S. E., & Marcq, E. 2015, Icar, 253, 1
Lee, Y. J., Titov, D. V., Tellmann, S., et al. 2012, Icar, 217, 599
Luginin, M., Fedorova, A., Belyaev, D., et al. 2016, Icar, 277, 154
Mallama, A., Wang, D., & Howard, R. A. 2006, Icar, 182, 10
Marcq, E., Belyaev, D., Montmessin, F., et al. 2011, Icar, 211, 58
Marcq, E., Bertaux, J.-L., Montmessin, F., & Belyaev, D. 2013, NatGe, 6, 25
Markiewicz, W. J., Petrova, E., Shalygina, O., et al. 2014, Icar, 234, 200
Marov, M. Y. 1978, ARA&A, 16, 141
Mayer, B., & Kylling, A. 2005, ACP, 5, 1855
McEwen, A. S. 1986, JGR, 91, 8077
Mills, F. P., Esposito, L. W., & Yung, Y. L. 2007, in Exploring Venus as a Terrestrial Planet, ed. L. W. Esposito, E. R. Stofan, & T. E. Cravens (Washington, D. C.: AGU), 73
Molaverdikhani, K., McGouldrick, K., & Esposito, L. W. 2012, Icar, 217, 648
Nakamura, M., Imamura, T., Ishii, N., et al. 2016, EP&S, 68, 75
Ogohara, K., Kouyama, T., Yamamoto, H., et al. 2012, Icar, 217, 661
Palmer, K. F., & Williams, D. 1975, ApOpt, 14, 208
Petrova, E. V., Shalygina, O. S., & Markiewicz, W. J. 2015a, P&SS, 113, 120
Petrova, E. V., Shalygina, O. S., & Markiewicz, W. J. 2015b, Icar, 260, 190
Pollack, J. B., Ragent, B., Boese, R., et al. 1979, Sci, 205, 76
Pollack, J. B., Toon, O. B., Whitten, R. C., et al. 1980, JGR, 85, 8141
Ragent, B., Esposito, L. W., Tomasko, M. G., Marov, M. I., & Shari, V. P. 1985, AdSpR, 5, 85
Ross, F. E. 1928, ApJ, 68, 57
Rossi, L., Marcq, E., Montmessin, F., et al. 2015, P&SS, 113–114, 159
Satoh, T., Ohtsuki, S., Iwagami, N., et al. 2015, Icar, 248, 213
Seiff, A., Schofield, J. T., Kliore, A. J., Taylor, F. W., & Limaye, S. S. 1985, AdSpR, 5, 3
Shalygina, O. S., Petrova, E. V., Markiewicz, W. J., Ignatiev, N. I., & Shalygin, E. V. 2015, P&SS, 113, 135
Shkuratov, Y., Kaydash, V., Korokhin, V., et al. 2011, P&SS, 59, 1326

Takada, J., Senda, S., Hihara, H., et al. 2007, Proc. IEEE International Conf. on Geoscience and Remote Sensing Symposiusm (New York: IEEE), 479
Titov, D. V., Bullock, M. A., Crisp, D., et al. 2007, in Exploring Venus as a Terrestrial Planet, ed. L. W. Esposito, E. R. Stofan, & T. E. Cravens (Washington, D. C.: AGU), 121
Titov, D. V., Markiewicz, W. J., Ignatiev, N. I., et al. 2012, Icar, 217, 682
Titov, D. V., Piccioni, G., Drossart, P., & Markiewicz, W. J. 2013, in Towards Understanding the Climate of Venus, ISSI Scientific Report Series, Vol 11, ed. L. Bengtsson et al. (New York: Springer), 23
Toon, O. B., Pollack, J. B., & Turco, R. P. 1982, Icar, 51, 358
Travis, L. D. 1975, JAtS, 32, 1190
Vandaele, A. C., Hermans, C., & Fally, S. 2009, JQSRT, 110, 2115
Wiscombe, W. J. 1980, ApOpt, 19, 1505
Woods, T. N., Chamberlin, P. C., Harder, J. W., et al. 2009, GeoRL, 36, L01101
Wright, W. H. 1927, PASP, 39, 220
Zasova, L. V., Ignatiev, N., Khatuntsev, I., & Linkin, V. 2007, P&SS, 55, 1712
Zasova, L. V., Krasnopolskii, V. A., & Moroz, V. I. 1981, AdSpR, 1, 13